SUPPLEMENTARY MATERIALS

Experimental details

These experiments based on condensates of ^{87}Rb operate with a fixed atomic scattering length a and a nearly fixed particle number. For the studies in the main text (Fig. 2 and Fig. 3), the characteristic collective interaction strength U is only weakly altered by a change of the trapping potential, whereby the density is increased for the data of Fig. 3 (with a stiffer trap having a trapping frequency of 60 Hz along the direction of imparted momentum) as compared to Fig. 2 (based on a looser, essentially single-beam trap having a trapping frequency of $\sim$10$-$15 Hz along the direction of imparted momentum). A larger variation of the ratio of Hamiltonian parameters U and J is achieved by directly modifying the tunneling energy J and investigating dynamics at equivalent times in units of the tunneling time $\hbar/J$.

Tunneling calibration

For all experimental data runs, we calibrated the value of tunneling by independently measuring two-site Rabi oscillations. That is, we turn on a single tunneling link for a range of evolution times and fit the resulting Rabi oscillation dynamics to obtain the effective tunneling rate. This is performed in the strong-tunneling limit, to minimize the influence of the mean-field interactions on the observed rate of tunneling. We then generate the frequencies for a lattice experiment under identical experimental conditions (voltages, laser powers), scaling the tunneling amplitudes according to the calibration. We run calibrations immediately before and after each data set, and the quoted tunneling values relate to the mean of the two calibration values, to account for drifts over time. The quoted tunneling errors relate to the standard error of the mean, incorporating the uncertainty (standard error of the fit of the Rabi oscillations) for each individual calibration.

Initialization of two-site superpositions

For the data in Fig. 3, we initialized the system with equal populations at sites 0 and -1. We apply a step-function $\pi/2$ pulse to the $0 \leftrightarrow -1$ tunneling link (evolving for one quarter of a Rabi period), also applying a controlled phase shift within the range $\phi/\pi = [-1, 0.9]$ (in steps of 0.1). In all cases, the two-site superposition states acquire an additional relative phase shift of -0.85π due to interactions during the initialization process, as determined by a comparison of the results to simulations in the high-tunneling limit. This leaves us with initialized states characterized by relative phase terms $\phi/\pi = [-0.95, 0.95]$. For presentation purposes, we map the data onto a redundant range with span 4π, copying data in the range $\phi/\pi = [0.05, 0.95]$ to $\phi/\pi = [-1.95, -1.05]$ and copying data in the range $\phi/\pi = [-0.95, -0.05]$ to $\phi/\pi = [1.05, 1.95]$.

Numerical simulations

We compare the experimental data to simulations based on the nonlinear Schrödinger equation (NLSE), alternatively referred to in the text as the Gross-Pitaevskii equation (GPE), with mean-field nonlinearities capturing the influences of atomic interactions. We utilize simulations of varying levels of complexity, opting for the simplest description capable of capturing the key experimental observations for each study. These analyses involve (1) solving a simple NLSE of 21 discrete modes with a uniform interaction energy to capture the self-trapping transition observed in Fig. 2 and (2) solving a real-space 1D NLSE that additionally incorporates the influences of the real-space trapping potential and the inhomogeneous and time-evolving atomic density to capture the phase-driven dynamics of Fig. 3.

Discrete-mode Gross-Pitaevskii simulations

The simulation curves accompanying the experimental data in Fig. 2 reflect the results of a NLSE with 21 discrete momentum modes. This classical mean-field simulation is justified by the macroscopic populations of the momentum modes in the experiments, with the number of atoms greatly exceeding the number of coupled momentum modes. For concreteness, we solve the dynamics of the (normalized) wave functions under the equations

$$i\hbar\dot{\psi_j} = -J(\psi_{j-1} + \psi_{j+1}) + U\sum_{j'} g_{j,j'}|\psi_{j'}|^2\psi_j \ , \quad \text{(S1)}$$

where $g_{j,j'} = 2 - \delta(j - j')$. This term reflects the different strengths of intra-mode and inter-mode interactions [43]. The exact difference by a factor of 2 reflects a simplifying approximation, whereby we assume the momentum modes to be perfectly distinguishable. This approximation, which neglects the influence of screening, is strictly valid when $2U \ll 4E_r \approx h \times 8.10$ kHz, where $E_r = \hbar^2k^2/2M$ is the photon recoil energy. The term $U = Nu$ represents the collective interaction, and normalization imposes $\sum_j |\psi_j|^2 = 1$. Implicit in this applied form is the projection of the full interaction Hamiltonian onto the modes comprising the 1D synthetic lattice. This maintains mode-conserving (forward) collisions but ignores mode-changing collisions that would populate states outside of the considered synthetic lattice state space [35]. We note that the forward collision rate

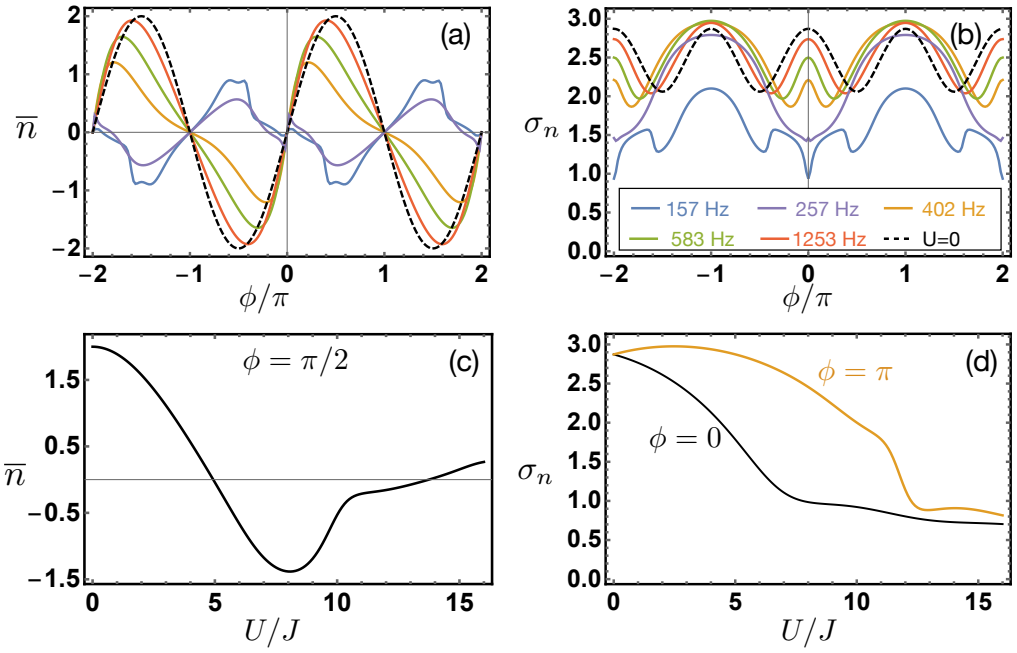

FIG. S1. **Discrete-mode Gross–Pitaevskii simulations of phase-driven dynamics in a 21-site lattice. (a,b)** Mean displacement $\bar{n}$ and distribution width σ_n vs. the initial relative phase ϕ of two-site superposition states after an evolution for two tunneling times. The curves relate to the same quantities presented in Fig. 3, but are based on simplified discrete-mode GP simulations that neglect the influence of the real-space trapping potential. The solid curves assume a homogeneous mean-field energy of $U/h = 1500$ Hz, and are evaluated for the tunneling values labeled in the legend in (b). For reference, dashed black lines denote the mean displacement $\bar{n}$ and distribution width σ_n vs. ϕ results for the non-interacting model. **(c)** The mean displacement $\bar{n}$ of the superposition state with an initial relative phase of $\pi/2$, plotted as a function of the interaction energy-to-tunneling energy ratio U/J (for an evolution over two tunneling times). **(d)** The distribution width σ_n of the superposition state with initial relative phases of 0 (black) and π (orange), plotted as a function of the interaction energy-to-tunneling energy ratio U/J (for an evolution over two tunneling times).

is dominant when $\rho\sigma v \ll g\rho$ (with σ the scattering cross section and v the relative velocity of scattering atoms), or equivalently when the relative k-vector of scattering atoms Δk is much less than $\hbar/a$, which is well satisfied for most of the cases explored.

While these simple discrete-mode simulations adequately describe the results of Fig. 2, they fail to capture several key features of the phase-driven dynamics data of Fig. 3. Specifically, as discussed in the main text, discrete-mode simulations that ignore the real-space trapping potential both predict an effective reversal of atomic current (sign flip of the CPR, $\bar{n}$ vs. ϕ) under interaction strengths close to the self-trapping regime and also predict that the distribution width σ_n should have ϕ-dependence that is symmetric with respect to $\phi = 0$.

Figure S1 summarizes the predicted behavior under the discrete-mode simulations. Figure S1(a, b) show the predicted curves for $\bar{n}$ vs. ϕ and σ_n vs. ϕ for the simple discrete-mode NLSE, which assumes a uniform interaction energy of $U = h \times 1500$ Hz. The curves are evaluated at the same values of J as considered in Fig. 3, with the curve assignments specified by the color legend in panel (b). For comparison, we also include the results for the non-interacting dynamics (dashed line, for $U = 0$).

While the non-interacting CPR in Fig. S1(a) is purely sinusoidal, in line with our expectations of the group velocity of a simple cosine band structure, the interacting simulation curves become more and more skewed as J is decreased. Furthermore, for the two smallest values of J considered, the CPR in fact reverses sign over a broad range of ϕ values. Or, more directly, the CPR gains a more intricate ϕ-dependence with several zero-crossings between $\phi = 0$ and $\phi = 2\pi$. To capture the dependence on the interaction energy-to-tunneling energy U/J, we summarize in Fig. S1(c) the dependence of $\bar{n}$ on ϕ for the exemplary superposition state with relative phase $\phi = \pi/2$. For this discrete-mode GP simulation, a reversal of $\bar{n}$ (and by extension a reversal of the group velocity) is predicted for increasing U/J, along with an overall damping of the magnitude of $\bar{n}$ as full self-trapping sets in. This intriguing behavior is not observed in experiment, and is found to be absent in the simulations that incorporate the influence of the real-space trapping potential (detailed below).

For the distribution width dependence on ϕ shown in Fig. S1(b), one again finds the expected dependence in the non-interacting limit. That is, viewing this as probing the evolution under the cosine band structure, equiva-

lent large widths are found when the dispersion is largest at the band center ($\phi = 0$) and band edge ($\phi = \pm\pi$), and the smallest widths are found at the points where the group velocity is nearly constant ($\phi = \pm\pi/2$). Interactions again significantly change the response of σ_n vs. ϕ. In particular, the discrete-mode simulations clearly depict the ϕ-dependent collapse of spreading that is seen in Fig. 3. First, for decreasing J (increasing U/J), one finds that the in-phase state with $\phi = 0$ undergoes a collapse of σ_n while the spreading of the out-of-phase state ($\phi = \pm\pi$) remains robust. The interaction-dependence is summarized in Fig. S1(d), where we plot the dependence of σ_n on the ratio U/J for the superposition states with $\phi = 0$ and $\phi = \pi$. Although these results are for a short evolution of just two tunneling times, there is an apparent difference in the responses of these two states, indicating a ϕ-dependent self-trapping transition that occurs at lower U/J values for the equal-phase superposition state as compared to the out-of-phase state.

Finally, we remark that further intricacies in the ϕ-dependence of σ_n can be seen in Fig. S1(b) for the $J/h = 157$ Hz curve. Additional local minima of σ_n are found (*i.e.*, near $\pm\pi/2$), seemingly coinciding with the appearance of additional features in the $J/h = 157$ Hz CPR curve in Fig. S1(a). While the investigation of this behavior lies outside of the scope of the present study, this hints at the instability of different superposition states to a collapse of spreading, perhaps with an interpretation in terms of a nonlinear band structure and its evolution under an increasing U/J ratio.

Real-space Gross-Pitaevskii simulations

As stated in the main text, a stiffer optical trapping condition was utilized for the data of Fig. 3 as compared to Fig. 2, to achieve a slight enhancement of the collective U (through enhancement of the atomic density). The higher trapping frequency of Fig. 3, and the correspondingly shorter trap period, had resulted in the trapping potential having a non-negligible influence on the momentum-space evolution during the experiments. To capture the influence of the trap, along with the resulting inhomogeneous atomic density, real-space simulations were performed.

In these numerical simulations, we treat the system as a 1D BEC in a harmonic trap under proper controlling laser fields. The simulation is done with dimensionless units by choosing the recoil momentum $\hbar k = \hbar \times 5.91 \times 10^6$ m^{-1} and energy $E_r = h \times 2.03$ kHz as the units for momentum and energy, and setting $\hbar = 1$. A complete run of simulations consists of the following three phases.

1. **Imaginary-time evolution**. The BEC ground state is achieved through imaginary-time evolution with a time-split-operator numerical method [84] and the ground-state energy is achieved to a precision up to $10^{-10} E_r$.

2. **Equal superposition state**. The coupling laser field is incorporated in real space and the zero-momentum ground state is adiabatically evolved into the desired initial states with equally populated momentum modes. A relative phase between two major momentum states is imprinted through adjusting the phase of the lasers fields.

3. **Wavepacket dynamics**. All real-space laser potentials are turned on, and the system is evolved (real-time evolution) up to two tunneling times before we achieve the final states.

In our simulation, the real space is sampled by 2^{15} points and the step in momentum space is $6.67 \times 10^{-3} \hbar k$. The time-evolution (both real and imaginary) step is $\delta t = 5 \times 10^{-5} \hbar / E_r$ (corresponding to 3.92×10^{-9} s), which ensures the convergence of the final states. The trapping frequency is 60 Hz and the mean interaction strength of the initial state takes a value of $U/h = 1568$ Hz as averaged over the whole trap. Finally, we confirm that our real-space GPE simulation agrees well with the tight-binding simulations when evaluated in the weak interaction and strong coupling limits.

For both the experimental data and simulation curves of Fig. 3, the evaluations of the expectation value and standard deviation of the displaced position in the synthetic lattice are restricted to a range of states that does not span the entire 21-site lattice. Specifically, those evaluations are performed over the site ranges of $\{-6, \ldots 5\}$ for the $J/h = 1253$ Hz and 583 Hz sets, $\{-5, \ldots 5\}$ for the $J/h = 402$ Hz set, $\{-4, \ldots 4\}$ for the $J/h = 257$ Hz set, and $\{-3, \ldots 3\}$ for the $J/h = 157$ Hz set.